MATERIALS CHEMISTRY FRONTIERS

RESEARCH ARTICLE

View Article Online
View Journal | View Issue

Cite this: *Mater. Chem. Front.*, 2025, **9**, 1758

B-site cation sequencing in $SrMnO_3$ using iron for zinc–air battery electrocatalysis: a structural evaluation†

Carolin Mercy Enoch,[a] Sagar Ingavale,[b] Prabakaran Varathan,[cd] Akhila Kumar Sahu[cd] and Anita Swami *[a]

Received 26th March 2025,
Accepted 11th April 2025

DOI: 10.1039/d5qm00268k

rsc.li/frontiers-materials

An unprecedented approach for synthesizing strontium manganese perovskite oxides (ABO_3) and their B-site substituted variants ($SrMn_{1-x}Fe_xO_3$) was employed using the molten salt synthesis route. This study aims to investigate the intrinsic property changes of perovskite oxide materials and their electrochemical response, particularly in the bifunctional oxygen reduction reaction (ORR) and oxygen evolution reaction (OER). Systematic substitution at the B-site induces a phase transition from hexagonal to trigonal, and then to orthorhombic, which was confirmed through Rietveld refinement of XRD data, along with SEM, TEM and XPS analyses. The multiple oxidation states of manganese (Mn^{3+}/Mn^{4+}) and iron (Fe^{3+}/Fe^{2+}) at the B-site play a crucial role in redox reactions. Furthermore, the orthorhombic brownmillerite phase (Sr_2MnFeO_5) promotes the ORR even without conductive support, which is attributed to its intrinsic conductivity stemming from the specific distribution of oxygen vacancies. The favorable adsorption/desorption energies of oxygen intermediates are a result of regulated electron filling in the d orbitals. The $SrMn_{0.7}Fe_{0.3}O_3$ variant was evaluated as a bifunctional electrocatalyst, showing an onset potential of 0.99 V *vs.* RHE for the ORR, and demonstrated excellent performance in rechargeable zinc–air batteries (ZABs), with a high peak power density of 114 mW cm^{-2} and a long cycle life of over 262 hours, exhibiting a specific capacity of 680 mA h g^{-1}. The unique structural properties of $SrMn_{0.7}Fe_{0.3}O_3$ make it a promising candidate for ZAB applications.

1. Introduction

Utilizing renewable energy sources to drive the development of technologies such as fuel cells, regenerative fuel cells (RFC), and metal–air batteries has garnered considerable interest.[1,2] The efficiency of these energy devices, including in conversion and storage processes, largely depends on the kinetics of the electrochemical reactions involved.[3,4] Among these reactions the ORR and OER are important,[5,6] which are inherently sluggish and thereby limit overall system efficiency.[7–11] While platinum (Pt/C) and iridium oxide (IrO_2) exhibit favorable activity for the ORR and OER, respectively, their poor stability, scarcity and high cost severely restrict their practical applications.[12–16] Hence, there is a pressing need to develop highly active, durable and sustainable alternatives for the ORR and OER. In recent years, various functional materials such as transition metal oxides,[17–24] spinels,[25,26] and MXenes[27] have been explored. Notably, perovskite-type oxides (ABO_3) have emerged as promising candidates due to their specific structure, wherein the 'A' site can host alkaline earth metals and the 'B' site can accommodate transition metals. This structural flexibility makes perovskites suitable for catalyzing sluggish electrochemical oxygen-based reactions. Materials like $LaNiO_3$[28] and BSCF ($Ba_{0.5}Sr_{0.5}Co_{0.8}Fe_{0.2}O_{3-\delta}$)[29,30] have demonstrated ORR and OER activities approaching those of noble metal catalysts. The design of effective perovskite oxide catalysts hinges on strategic principles such as 'A' site doping,[31] 'B' site doping,[31–33] and creation of oxygen vacancies.[34,35] Substituting 'A' and 'B' sites with different redox-active elements can finely tune the structural and chemical properties of these materials, thereby enhancing their catalytic activity. 'B' site doping, in particular, influences oxygen diffusion kinetics, as exemplified by $BaFe_{1-x}Bi_xO_{3-\delta}$[36–39] and $BaFe_{0.9}Sn_{0.05}O_{3-\delta}$[40] in the case of the ORR. Furthermore, Mn-doped ABO_3-type oxides have shown excellent ORR activity

[a] *Department of Chemistry, SRM Institute of Science and Technology, Kattankulathur 603203, Chennai, India. E-mail: swamians@srmist.edu.in, swami.anita@gmail.com*
[b] *Department of Chemical Engineering, Faculty of Engineering, Chulalongkorn University, Bangkok 10330, Thailand*
[c] *CSIR – Central Electrochemical Research Institute – Madras Unit, CSIR Madras Complex, Taramani, Chennai 600 113, India*
[d] *Academy of Scientific and Innovative Research (AcSIR), Ghaziabad 201002, India*

† Electronic supplementary information (ESI) available. See DOI: https://doi.org/10.1039/d5qm00268k

due to a moderate interaction between the intermediate and the catalyst surface, governed by the average valence of Mn^{4+}/Mn^{3+}.[41] Incorporating Mn or other redox-active elements into ABO_3-type oxides has been studied to improve OER/ORR activity by modifying the electronic structure and reducing the adsorption energies of the intermediates.[35,42,43] Recent studies highlight the enhancement of catalytic activity by doping Mn into $LaCoO_3$ and optimizing Co^{3+}/Co^{2+} ratios to promote the OER.[44] Similarly, doping Sr into LMN ($LaNi_{0.5}Mn_{0.5}O_3$) enhances catalytic activity through particle size reduction and surface Ni trivalency, crucial for the ORR and OER in alkaline media.[45] Doping has been extensively studied as a potential method to replace classic noble metal catalysts. Nitrogen-doped carbon was selected as the catalyst model for the ZAB electrode, showing remarkable stability with 650 cycles of discharging/charging at a high rate of 25 mA cm^{-2}.[46] A carbon nanosheet doped with iron and nitrogen was successfully documented, as it contains active Fe–N_x sites. Fe,N-CNS exhibited stable charge/discharge potentials of 1.96/1.04 V after 60 cycles, with minimal voltage drop.[47] The hexagonal oxide $Ba_4Sr_4(Co_{0.8}Fe_{0.2})_4O_{15}$ (hexBSCF), featuring unique tetrahedral and octahedral Co/Fe coordinations, exhibits extraordinary activity for the OER. When tested in an electrochemical cell, the hexBSCF catalyst displayed a low overpotential of approximately 340 mV at a current density of 10 mA cm^{-2} and a small Tafel slope of 47 mV dec^{-1} in 0.1 M KOH solution, demonstrating the highest OER activity ever reported among metal oxides.[48] The specific La/Fe co-doped structure is the primary origin of the high bifunctional catalytic activity, as co-doping enhances the catalytic activity of the nanoparticles for both the ORR and OER. Density functional theory (DFT) calculations show that La/Fe co-doping decreases the overpotentials of both reactions and improves the stability of the nanoparticles against corrosion. Additionally, the carbon coating on $La_{0.23}Fe_{0.15}$–Co_3O_4/NCNTs helps reduce activity losses caused by electrical resistance during catalytic processes, further enhancing ORR and OER activities.[49]

In our study, we present the rational design of strontium manganese perovskite oxide ($SrMnO_3$) with 'B' site variations involving Fe, resulting in significantly enhanced electrocatalytic activity for the ORR and OER. Increasing Fe content in $SrMn_{1-x}Fe_xO_3$ (where x = 0.2, 0.3, 0.5) transitions the crystal system from hexagonal to trigonal while preserving the perovskite structure. The trigonal phase of $SrMn_{0.7}Fe_{0.3}O_3$ possesses an onset potential (E_{onset}) of 0.99 V *vs.* RHE and demonstrates high stability, while Sr_2MnFeO_5 adopts an orthorhombic brownmillerite-like structure due to orderly removal of oxide ions, leading to controlled oxide ion vacancies. The superior activity and stability of the Fe-doped series stem from the synergy between Fe^{4+}/Fe^{3+} and an equal proportion of iron and manganese in the 'B' site, creating crystal defects. The optimized composition of Sr_2MnFeO_5 achieved an E_{onset} and a half-wave potential ($E_{1/2}$) of 0.89 V and 0.71 V *vs.* RHE, respectively, in O_2-saturated 0.1 M KOH solution. Moreover, owing to its intrinsic conductivity, Sr_2MnFeO_5 exhibits excellent ORR catalytic performance even without additional conducting additives. The $SrMn_{0.7}Fe_{0.3}O_3$ variant was also demonstrated to be a promising candidate for ZAB applications with a long cycle life and a specific capacity of 262 hours and 680 mA h g^{-1}, respectively. Thus, the study demonstrates that engineering perovskite oxides offers a promising pathway for designing dynamic electrocatalysts for the ORR and OER, leveraging structural modifications and elemental doping strategies to enhance catalytic performance.

2. Experimental section

2.1. Materials

Strontium nitrate ($Sr(NO_3)_2$), manganese nitrate ($Mn(NO_3)_2$), iron nitrate nonahydrate ($Fe(NO_3)_3{\cdot}9H_2O$), Nafion as a binder (5 wt% solution), and potassium hydroxide (KOH) pellets were obtained from Sigma-Aldrich. Alkali metal salts like KCl and NaCl, ethanol and isopropyl alcohol were obtained from SRL (Sisco Research Laboratories Pvt. Ltd), India. All chemicals were used without any additional purification. Milli-Q water with a resistance of 18.2 MΩ cm was used in both experiments and electrochemical assessments.

2.2. Synthesis of B-site substituted strontium manganese perovskite oxide

Oxygen-deficient strontium manganese and iron perovskite oxide were synthesized using a molten-salt approach, with iron substituting manganese at the B-site. Strontium nitrate, manganese nitrate, and iron nitrate served as metal precursors to synthesize strontium manganese iron perovskite oxides with the formula $SrMn_{1-x}Fe_xO_3$ (where x = 0.2, 0.3, 0.5) and Sr_2MnFeO_5. Initially, the metal precursors were mixed in stoichiometric proportions with molten salt (NaCl and KCl) in a 1 : 5 ratio. The mixture was then transferred to a ball mill jar and milled at 600 rpm for 2 hours. Subsequently, the powder was collected and heated at 900 °C for 4 hours in an open air atmosphere. After cooling, the resulting samples were labeled as $SrMn_{0.8}Fe_{0.2}O_3$, $SrMn_{0.7}Fe_{0.3}O_3$, $SrMn_{0.5}Fe_{0.5}O_3$ and Sr_2MnFeO_5.

2.3. Materials characterization

The powder X-ray diffraction (XRD) patterns were acquired using a PANalytical X'pert Pro diffractometer with Cu K_α radiation (λ = 1.5406 Å, 40 kV, 40 mA), covering a 2θ range of 10–90° at a scan rate of 2° min^{-1}. Rietveld refinements were conducted using the FullProf Suite program (FP) and the EXPGUI interface to determine lattice parameters. Imaging using high-resolution scanning electron microscopy (HRSEM) was conducted on a Thermo Scientific Apreo S instrument with an acceleration voltage of 20 kV. Transmission electron microscopy (TEM) images were obtained using a JEOL JEM-2100 Plus transmission electron microscope operating at 200 kV with a thermionic LaB_6 electron source. TEM specimens were prepared by dissolving the powder in a mixture of water and isopropanol (at a volume ratio of 3 : 1). X-ray photoelectron spectroscopy (XPS) was performed using a Shimadzu ECSA 3400 device. The obtained XPS spectra were analyzed by deconvoluting and fitting them with a Shirley-type background function for further analysis.

2.4. Electrochemical measurements

To maintain optimal conditions for the working electrode, it was polished with 0.05 μm alumina slurry. To prepare the catalyst ink, 3 mg of the catalyst and 2 mg of Ketjenblack carbon (KBC) as a conductive additive were dispersed in 1 mL of ethanol. To this mixture, 50 μL of 5 wt% Nafion solution was added, and the mixture was sonicated for 40 minutes in a water bath.[50] Subsequently, the cleaned glassy carbon (GC) electrode surface (with a geometric area of 0.0707 cm^2) was coated with 4 μL of this catalyst ink, resulting in a catalyst loading of 0.28 mg cm^{-2}. Ultimately, the electrode was left to dry overnight at ambient temperature in an ethanol atmosphere and used as the working electrode for electrochemical measurements. For comparison, a commercial Pt/C (20 wt%) electrode was also prepared using a similar method, with an actual Pt loading of 0.17 mg cm^{-2}. For the intrinsically conductive electrode, 3 mg of the catalyst was dispersed in 1 mL of ethanol and 40 μL of 5 wt% Nafion was added, followed by sonication for 40 minutes in an ice bath. All electrochemical measurements were conducted using a CHI 760E potentiostat (CH Instruments, Inc., USA) in a three-electrode system in 0.1 M aqueous KOH solution at room temperature. A graphite rod served as the counter electrode and Ag/AgCl (saturated KCl) as the reference electrode. The calibration experiment was conducted using a typical three-electrode system in 0.1 M KOH electrolyte at room temperature, where pre-cleaned Pt wires were used as the working and counter electrodes, while an Ag/AgCl (with saturated KCl) electrode served as the reference electrode. Initially, the electrolyte solution was fully saturated with ultra-pure (99.99%) hydrogen gas before performing linear sweep voltammetry (LSV) at a scan rate of 1 mV s^{-1}. The point at which the current reaches zero is typically considered the thermodynamic potential for hydrogen electrode reactions, relative to the reference electrode (in this case, Ag/AgCl). In 0.1 M KOH electrolyte, the zero-current point occurs at −0.973 V *vs.* Ag/AgCl. Therefore, the potential of Ag/AgCl relative to the RHE was converted to the reversible hydrogen electrode (RHE) scale using the equation: $E(\mathrm{RHE}) = E(\mathrm{Ag/AgCl}) + 0.973$ V.[51] Prior to ORR measurements, the rotating disc electrode (RDE) surface was cleaned by cycling between −0.9 V and 0.1 V *vs.* Ag/AgCl in N_2-saturated 0.1 M KOH solution. Cyclic voltammetry (CV) was performed in both N_2- and O_2-saturated electrolytes, while LSV was conducted in an O_2-saturated electrolyte at a sweep rate of 10 mV s^{-1}. The ORR stability of the catalysts was evaluated by chronoamperometry at half-wave potential *vs.* Ag/AgCl in 0.1 M KOH electrolyte solution. For rotating ring disc electrode (RRDE) measurements, 10 μL of the prepared ink was drop-coated onto a 4 mm diameter working electrode (with a geometric area of 0.1256 cm^2). The disk electrode was scanned at 10 mV s^{-1}, while the ring potential was held constant at 0.5 V *vs.* Ag/AgCl. The production of peroxide (HO_2^-) and the number of electrons transferred (n) were, respectively, calculated using the following formulae:

$$\%HO_2^- = 200 \times \frac{I_r/N}{I_d + I_r/N} \quad (1)$$

$$n = 4 \times \frac{I_d}{I_d + I_r/N} \quad (2)$$

where I_d is the disk current, I_r is the ring current and N is the current collection efficiency of the Pt ring (here $N = 0.38$).[52]

The mean number of e_g electrons can be measured using the following equation:[53]

$$n = -\frac{1}{m}\sum_{Mn,Fe} e_g^d \times p \quad (3)$$

where m is the number of transition metal elements at the B-site, e_g^d represents the occupation numbers of Mn and Fe ions at different valence states in the e_g orbital and p represents the percentage of various valence states calculated by XPS (Fig. 5). The electrochemically active surface area (ECSA) was determined by recording CVs in the non-faradaic region (1.1 to 1.30 V *vs.* RHE) at various scan rates in 0.1 M KOH electrolyte under N_2 saturation. The double-layer capacitance, measured at 1.20 V *vs.* RHE, is directly proportional to the ECSA. The mass activity (A mg^{-1}) was calculated from eqn (4) using mass loading $M = 0.02$ mg.

$$\text{Mass activity} = \frac{I_k}{M} \quad (4)$$

The specific activity (mA cm^{-2}) was calculated from the values of ECSA using eqn (5):

$$\text{Specific activity} = \frac{I_k}{S} \quad (5)$$

The fabrication, assembly, and testing of ZAB involve detailed steps to ensure optimal performance. A commercial zinc sheet with a thickness of 0.3 mm was used as the anode, while the cathode consists of optimized catalysts $SrMn_{0.7}Fe_{0.3}O_3$ and $SrMn_{0.5}Fe_{0.5}O_3$ applied onto a gas-permeable layer (GDL BC39). The catalyst ink was prepared by mixing adequate amounts of the catalyst, KBC, isopropyl alcohol (IPA), and Nafion, followed by one hour of sonication to obtain a homogeneous mixture. The admixture was then brush-coated onto the GDL surface layer by layer until a loading of 1 mg cm^{-2} was achieved. A 6 M aqueous solution of KOH served as the electrolyte, facilitating ionic conduction between the electrodes. During assembly, the zinc anode and the coated cathode were placed into a cell with an active area of 1 cm^2, ensuring proper separation to prevent short circuits, and the electrolyte is added before sealing the cell. The cathode side of the cell configuration was in contact with the air in the atmosphere, and hence this is an air breathing ZAB. The performance of the ZAB was evaluated using a Biologic VSP/VMP 3B-20 electrochemical workstation. Cell polarization of ZAB provides critical insights into its overpotential and operational limits as well as the kinetic barriers associated with the electrochemical reactions. Galvanostatic discharge curves were recorded at a constant current density of 25 mA cm^{-2} to evaluate the ZAB's voltage stability.[54]

$$\text{Specific capacity } (\text{mA h g}^{-1}) = \frac{I \times t}{\text{Mass of the active material}} \quad (6)$$

here I is the current (in mA), t is the discharge time (in hours), and the unit of the mass of the active material used is grams. Rate capability tests were conducted across current densities ranging from 5 to 40 mA cm^{-2} to assess performance under different loads, and charge–discharge cycling was carried out at 5 mA cm^{-2} at 10-minute intervals to evaluate long-term stability. ΔE represents the difference in voltage between the charge and discharge processes during cycling, which indicates the voltage losses associated with the ZAB operation.[55]

$$\Delta E = V_{\text{charge}} - V_{\text{discharge}} \quad (7)$$

All tests were conducted at room temperature (25 °C) and ambient pressure to ensure accurate reflection of the battery's performance in practical applications.

Turnover frequency (TOF) is used to measure the number of active sites on the catalyst and was calculated using the formula:

$$\text{TOF} = \frac{j \times a}{4 \times n \times F} \quad (8)$$

where j is the current density at a given potential, a is the surface area of the electrode, n is the number of moles of the catalyst, and F is the Faraday constant.

3. Results and discussion

The effect of B-site substitution on strontium manganese perovskite oxide was evaluated through structural and morphological techniques using XRD, TEM and SEM. A series of Fe-substituted strontium manganese perovskite oxides were synthesized by precisely controlling the Fe content at the B-site *via* molten salt synthesis. The XRD patterns of $SrMnO_3$ and its variants with iron dopants ($SrMn_{0.8}Fe_{0.2}O_3$, $SrMn_{0.7}Fe_{0.3}O_3$, $SrMn_{0.5}Fe_{0.5}O_3$ and Sr_2MnFeO_5), shown in Fig. S1 (ESI†), indicated highly crystalline phases where Mn ions were successfully replaced by Fe ions at the B-site of the structure. Upon the addition of Fe, all samples exhibited similar patterns to $SrMnO_3$, with diffraction peaks gradually shifting to lower angles (as evidenced by the peak at 32.7°), consistent with an increase in the covalent radius due to substitution of Mn^{3+} ions (0.58 Å) by Fe^{3+} ions (0.76 Å). This confirms that, in all compounds, the B-site was substituted by Fe according to the ratio of precursor salts used in synthesis. Detailed *hkl* plane information for all samples is tabulated in Table S1 (ESI†). Rietveld analysis using the FullProf software suite was conducted to understand structural features and crystal symmetries, with refined parameters and resultant profiles provided in Table S2 (ESI†). Based on the refinement shown in Fig. 1, $SrMn_{0.8}Fe_{0.2}O_3$, $SrMn_{0.7}Fe_{0.3}O_3$, and $SrMn_{0.5}Fe_{0.5}O_3$ exhibit a trigonal phase with the space group $R\bar{3}c$ (space number: 167), whereas Sr_2MnFeO_5 displays an orthorhombic phase. Table S2 (ESI†) offers the refined structural information including lattice parameters, space groups, space group numbers, and R factors (reliability factors) such as Chi^2 (χ^2) and residual parameters. To gain deeper insights into the crystalline structure and occupancies of the synthesized materials, unit cell parameters obtained from the refined results were

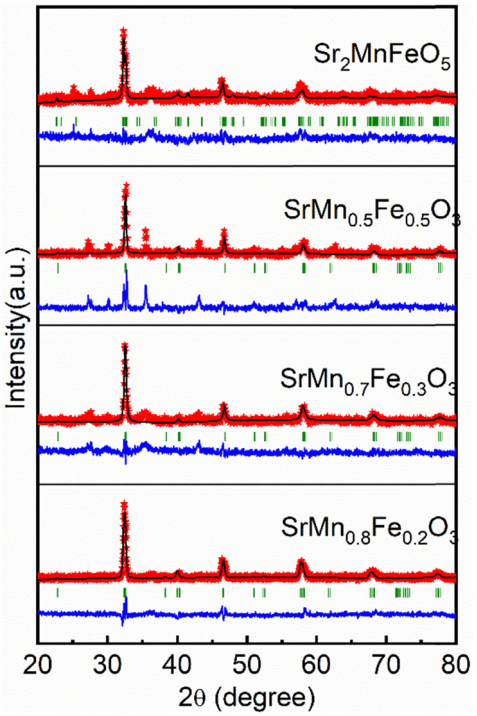

Fig. 1 Rietveld refinement powder XRD patterns of $SrMn_{0.8}Fe_{0.2}O_3$, $SrMn_{0.7}Fe_{0.3}O_3$, $SrMn_{0.5}Fe_{0.5}O_3$ and Sr_2MnFeO_5. The pink stars portray the observed profile, the black line depicts the calculated profile, the green upward markers indicate the Bragg diffraction positions, and the blue line at the bottom shows the disparity between the observed profile and the calculated profile.

analyzed. The structures are illustrated in Fig. 2(a)–(e). It is evident that the sequential substitution of Fe at the manganese site occurs in accordance with the percentage. In $SrMn_{0.8}Fe_{0.2}O_3$ ($x = 0.2$), the original trigonal phase with a hexagonal setting (a = 5.5289 Å, b = 5.5289 Å, c = 13.4367 Å) of the perovskite oxide is maintained. Similarly, at $x = 0.3$ ($SrMn_{0.7}Fe_{0.3}O_3$, a = 5.5607 Å, b = 5.5607 Å, c = 13.4142 Å) and $x = 0.5$ ($SrMn_{0.5}Fe_{0.5}O_3$, a = 5.5075 Å, b = 5.5075 Å, c = 13.4167 Å), the trigonal phase persists. However, when Mn and Fe contents are in equal proportions, a transition to an orthorhombic brownmillerite phase, Sr_2MnFeO_5 (a = 5.5591 Å, b = 15.7079 Å, c = 5.4918 Å, JCPDS card no. 50-0297), is observed. The distinctive feature of this structure is the alternating sequence of octahedral $(MnFe)O_6$ and tetrahedral $(MnFe)O_4$ layers with ordered oxygen vacancies, as depicted in Fig. 2(e). This arrangement of Mn and Fe ions in the B-site of stoichiometric $SrMnO_3$ results in the formation of nonstoichiometric Sr_2MnFeO_5, characterized by ordered oxygen vacancies that enhance oxygen ion mobility and exchange kinetics.

The morphological aspects of $SrMnO_3$ and Fe-substituted $SrMnO_3$ were studied using SEM, as shown in Fig. 3 and Fig. S2 (ESI†). Pristine $SrMnO_3$ (Fig. S2(a) and (b), ESI†) presents uniform hexagonal rods with an average diameter of 8 μm and lengths ranging from 10 to 15 μm. Significant changes in morphology were observed when Mn was substituted by Fe and when the Fe content increased in the composite. $SrMn_{0.8}Fe_{0.2}O_3$ (Fig. 3(a) and (b)) showed only aggregated tiny particles of various

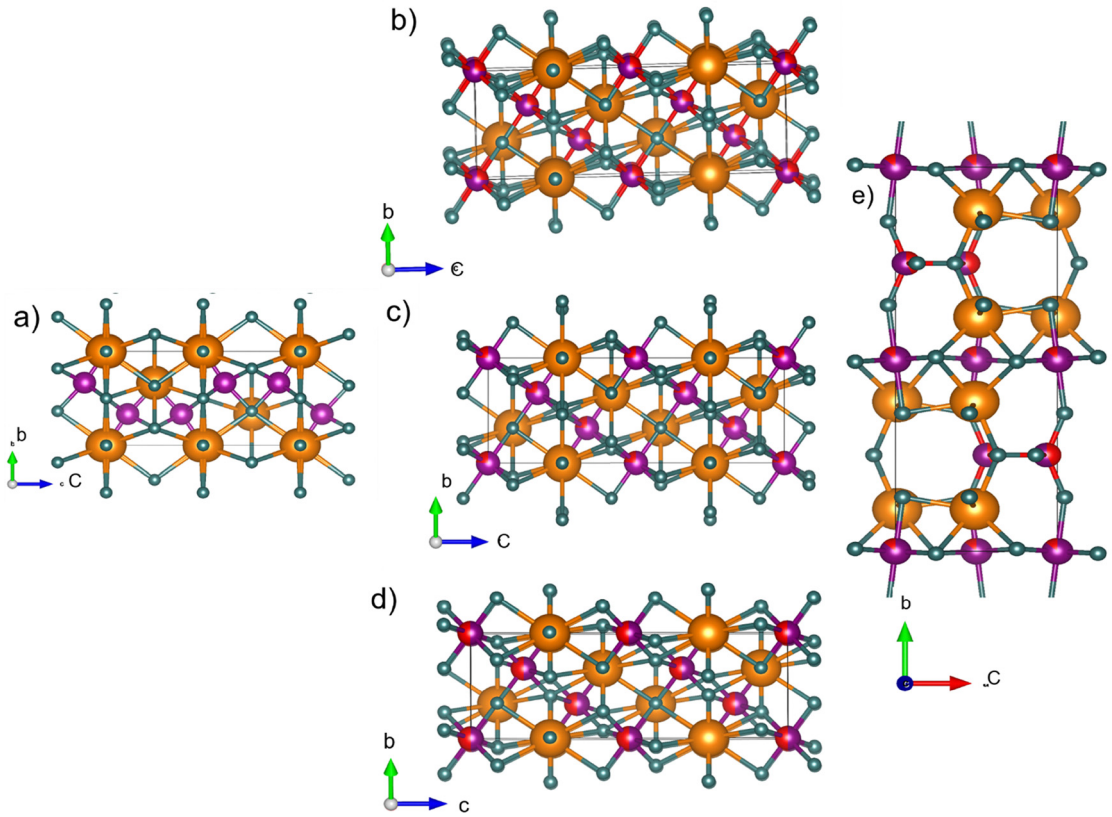

Fig. 2 Structural representation of (a) $SrMnO_3$, (b) $SrMn_{0.8}Fe_{0.2}O_3$, (c) $SrMn_{0.7}Fe_{0.3}O_3$, (d) $SrMn_{0.5}Fe_{0.5}O_3$ and (e) Sr_2MnFeO_5. Orange balls represent strontium; red balls represent iron; purple balls represent manganese and cyan green balls represent oxygen.

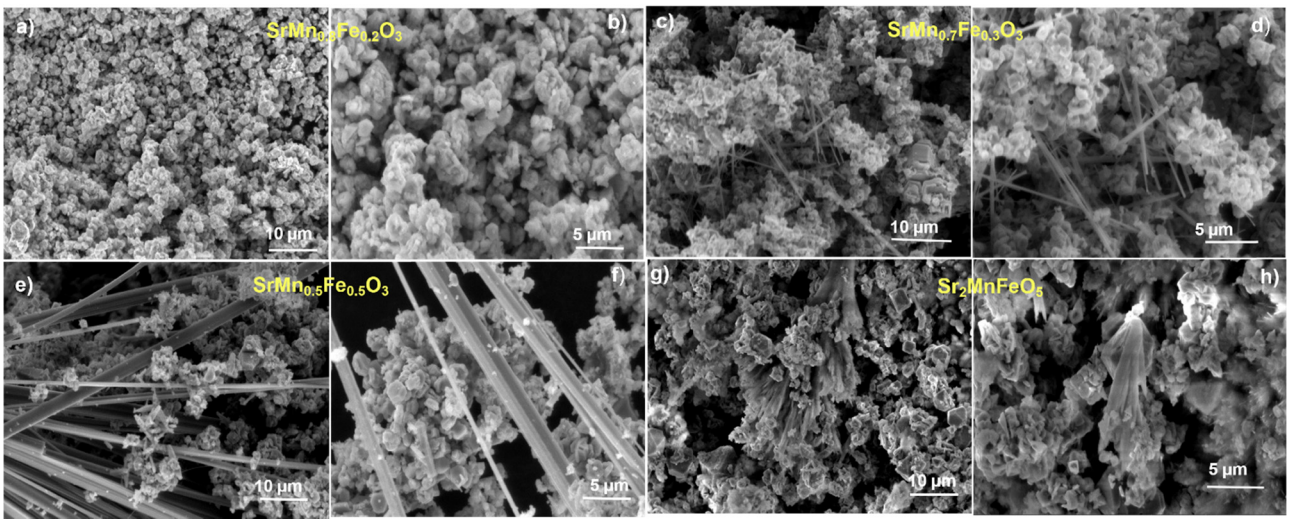

Fig. 3 SEM images of (a) and (b) $SrMn_{0.8}Fe_{0.2}O_3$, (c) and (d) $SrMn_{0.7}Fe_{0.3}O_3$, (e) and (f) $SrMn_{0.5}Fe_{0.5}O_3$ and (g), (h) Sr_2MnFeO_5 recorded at different magnifications.

magnitudes and shapes. In the case of $SrMn_{0.7}Fe_{0.3}O_3$ (Fig. 3(c) and (d)), nanorods more than 20 μm long were embedded in the particle aggregates, which further increased in size with increasing Fe content, as seen in $SrMn_{0.5}Fe_{0.5}O_3$ (Fig. 3(e) and (f)). Additionally, the Sr_2MnFeO_5 sample (Fig. 3(g) and (h)) exhibited a distinct morphology where particles and rod-shaped structures seemed to merge completely, forming comparatively flat structures. Fig. S3 (ESI†) displays energy dispersive X-ray (EDX) spectra substantiating the presence of Sr, Fe and Mn in all the samples. TEM and HRTEM images, and selected area electron diffraction

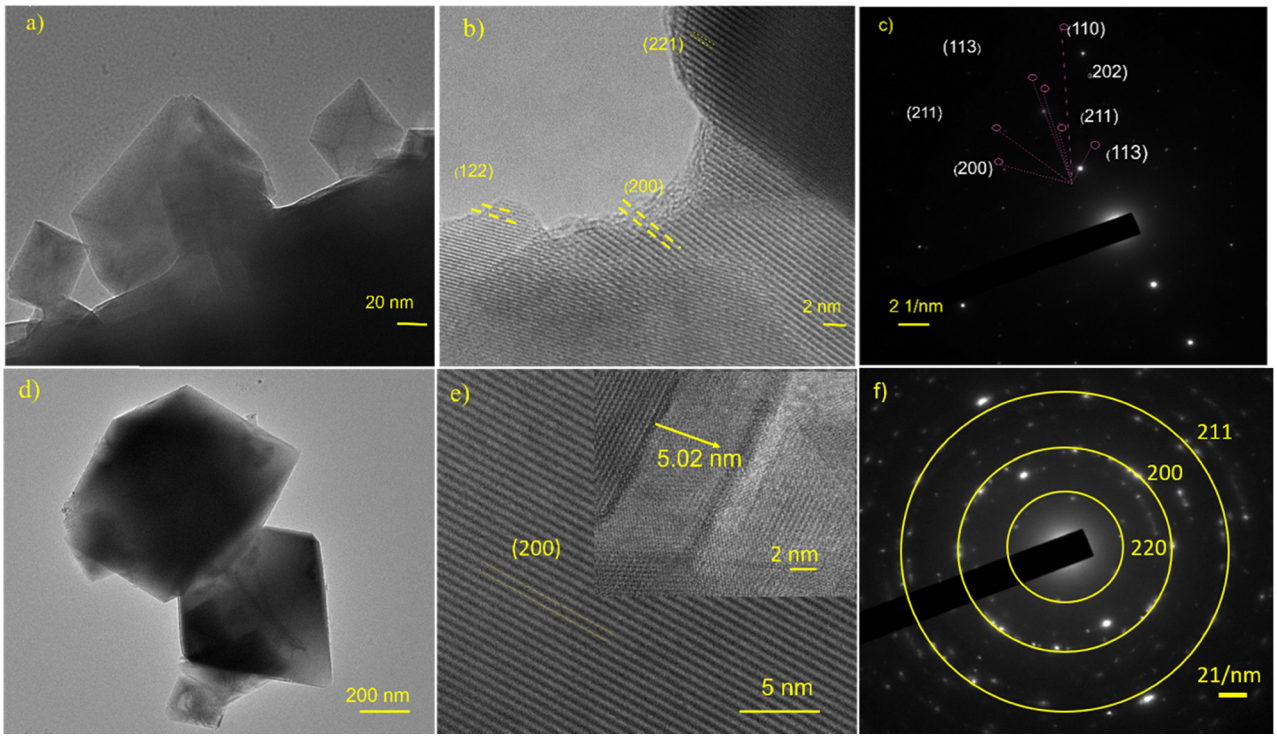

Fig. 4 (a) TEM image, (b) HRTEM image displaying the lattice planes corresponding to (122), (221) and (200) and (c) SAED pattern of $SrMn_{0.7}Fe_{0.3}O_3$; (d) TEM image, (e) HRTEM images showing the lattice plane (200) and (f) SAED pattern of Sr_2MnFeO_5.

(SAED) patterns of $SrMn_{0.7}Fe_{0.3}O_3$ and Sr_2MnFeO_5 are shown in Fig. 4(a)–(f). The presence of specific lattice planes in the images, along with the indexed planes from the SAED pattern, confirms their corresponding composition. To examine the electronic structure and chemical state of the constituent elements, XPS analysis was performed for the optimized sample $SrMn_{0.7}Fe_{0.3}O_3$. Fig. 5(a) shows the deconvoluted Sr 3d core level spectrum displaying the spin–orbit coupled $3d_{3/2}$ and $3d_{5/2}$ peaks at 135.1 eV and 133.3 eV, respectively, with an energy separation of 1.8 eV. The Mn 2p doublet, Mn $2p_{1/2}$ and Mn $2p_{3/2}$, in Fig. 5(b) can be split into two peaks each, fitted at 641.7 eV, 643.13 eV, 653.3 eV, and 654.7 eV, which are assigned to Mn^{3+} ($2p_{3/2}$), Mn^{4+} ($2p_{3/2}$), Mn^{3+} ($2p_{1/2}$), and Mn^{4+} ($2p_{1/2}$), respectively. The ratio of the Mn^{3+} to Mn^{4+} redox peaks observed in the XPS spectrum influences both the ORR and the OER. This ratio determines the amount and rate of adsorption and desorption of OH^- species on the catalyst surface, which in turn regulates the rate of oxygen-related reactions. The Fe 2p doublet, Fe $2p_{3/2}$ and Fe $2p_{1/2}$, shown in Fig. 5(c), can be deconvoluted into four peaks, fitted at 711.0 eV, 713.09 eV, 723.9 eV, and 725.8 eV, assigned to Fe^{2+} ($2p_{3/2}$), Fe^{3+} ($2p_{3/2}$), Fe^{2+} ($2p_{1/2}$), and Fe^{3+} ($2p_{1/2}$), respectively. The peak positions depend on the oxidation state and local coordination of the Fe atoms in the sample. The O 1s XP spectrum of the $SrMn_{0.7}Fe_{0.3}O_3$ perovskite is shown in Fig. 5(d), depicting oxygen with three different electronic environments, with peaks positioned at 529.8 eV, 531.5 eV, and 532.3 eV. The peak with the least binding energy implies the lattice oxygen (O_L), the middle peak at 531.5 eV corresponds to Fe/Mn/O, and the highest binding energy peak is due to the presence of surface-adsorbed oxygen (O_{ad}). A higher amount of surface-adsorbed oxygen facilitates the electroreduction of oxygen. Additionally, the intrinsically conducting perovskite oxide Sr_2MnFeO_5 was analyzed by XPS. Fig. 5(e) shows the deconvoluted Sr 3d core level spectrum depicting the spin–orbit doublet Sr $3d_{3/2}$ and Sr $3d_{5/2}$, located at 133 eV and 131 eV, respectively. Three deconvoluted peaks in the Mn 2p spectrum at 645.5 eV, 643.0 eV, and 640.5 eV correspond to Mn^{4+}, Mn^{3+} and Mn^{2+}, respectively. The Fe 2p doublet, Fe $2p_{3/2}$ and Fe $2p_{1/2}$, can be deconvoluted into four peaks, fitted at 725.2 eV, 722.5 eV, 712.5 eV, and 709.0 eV, assigned to Fe^{3+} ($2p_{1/2}$), Fe^{2+} ($2p_{1/2}$), Fe^{3+} ($2p_{3/2}$), and Fe^{2+} ($2p_{3/2}$), respectively, as shown in Fig. 5(g). Table S3 (ESI†) presents the percentage of various oxidation states of Fe and Mn in both samples. The O 1s XP spectrum for the Sr_2MnFeO_5 perovskite is shown in Fig. 5(h). Two types of oxygen are seen in the O 1s spectrum at 531.5 eV and 530.1 eV, which can be assigned to O_{ad} and O_L, respectively.

The electrocatalytic activities of the as-prepared $SrMn_{1-x}Fe_xO_3$ perovskites towards the ORR and OER were investigated in 0.1 M KOH solution. The electrocatalytic performance of the electrodes was evaluated by CV, as presented in Fig. 6(a) and Fig. S4(a)–(d) (ESI†). N_2 saturated electrolyte displays no noticeable reduction peaks in the voltammogram, which is expected to be due to the absence of oxygen. In an O_2 saturated system, reduction current was observed for all the samples, $SrMn_{0.7}Fe_{0.3}O_3$, $SrMn_{0.8}Fe_{0.2}O_3$, $SrMn_{0.5}Fe_{0.5}O_3$ and $SrMnO_3$, which signifies the reduction of dissolved oxygen molecules in the electrolyte. Fig. 6(b) and Fig. S5 (ESI†) exemplify the comparison of LSVs. $SrMn_{0.7}Fe_{0.3}O_3$

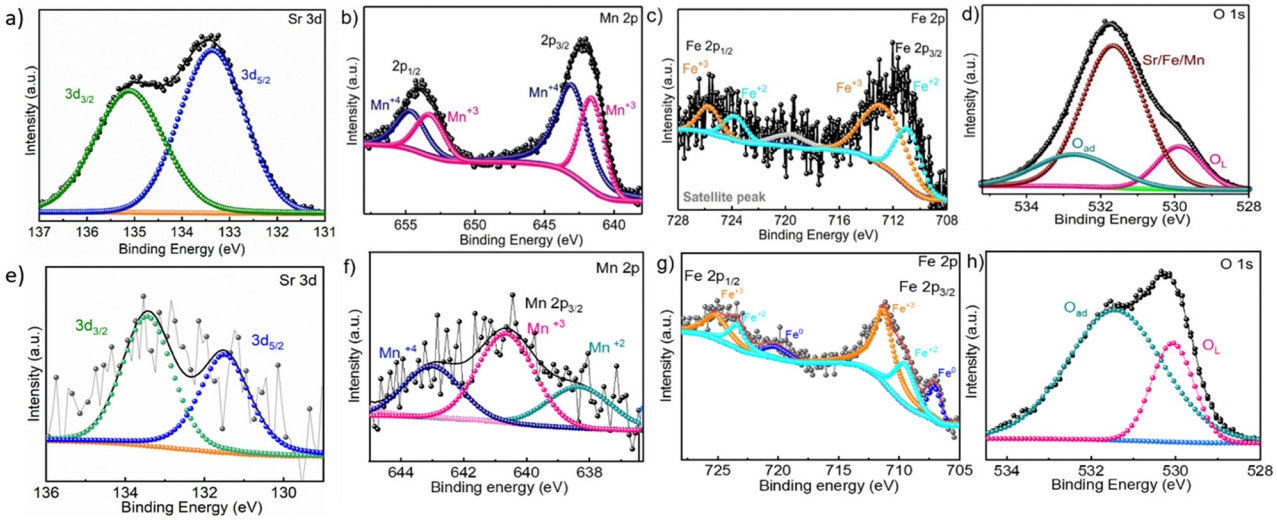

Fig. 5 Deconvoluted XP spectra of Sr 3d, Mn 2p, Fe 2p and O 1s in (a)–(d) $SrMn_{0.7}Fe_{0.3}O_3$ and (e)–(h) Sr_2MnFeO_5, respectively.

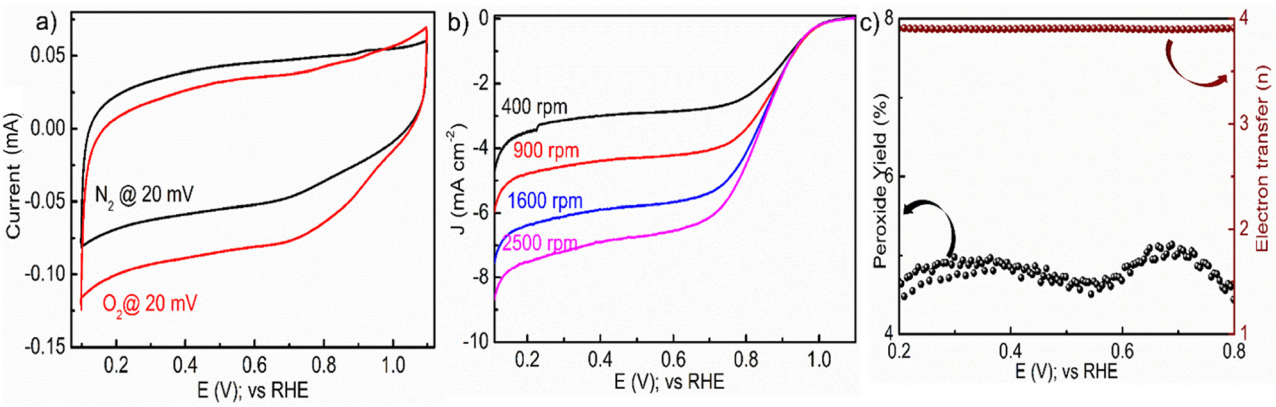

Fig. 6 (a) Cyclic voltammograms of $SrMn_{0.7}Fe_{0.3}O_3$ obtained in 0.1 M KOH solution saturated with N_2 and O_2 at a scan rate of 20 mV s^{-1}. (b) Linear sweep voltammograms recorded at 10 mV s^{-1} with various rotation rates. (c) RRDE measurement displaying the number of electrons transferred and peroxide yields.

exhibits an excellent ORR performance with an E_{onset} of 0.99 V and an $E_{1/2}$ of 0.84 V *vs.* RHE comparable to those of the commercial Pt/C (E_{onset} = 0.1 V and $E_{1/2}$ = 0.83 V) and most reported related materials in previous works (Table S9, ESI†). The list of E_{onset}, $E_{1/2}$ potential (V *vs.* RHE) and current density (mA cm^{-2}) values for all the samples is given in Table S4 (ESI†), which reveals that $SrMn_{0.7}Fe_{0.3}O_3$ exhibits better ORR activity than all the other catalysts, suggesting the optimized percentage of iron in the crystal. It was confirmed that all the samples are finely doped with iron according to the composition and show an improvement in the ORR catalytic activity compared with the undoped catalyst, which can be clearly seen in Fig. 7(a) and Fig. S5(a) (ESI†). In order to determine whether the ORR with all the catalysts occurs by four-electron ($4e^-$) reduction of oxygen to produce H_2O, LSV measurements were performed at different rotating speeds from 400 to 2500 rpm (Fig. S5, ESI†). With the increase of the rotational speed, the current density increased due to the fast diffusion rate. Furthermore, the Koutecky–Levich (K–L) equation was applied to calculate the electron-transfer number (n) in the case of all the catalysts (Fig. 7(b)). The 'n' was calculated to be 3.9 for all the catalysts, suggesting the $4e^-$ oxygen reduction pathway. In addition, the corresponding RRDE measurements were also employed for the catalysts (as shown in Fig. 6(c) and Fig. S6(a)–(d), ESI†) to confirm the reaction pathways towards oxygen reduction. The HO_2^-% yield and 'n' calculated from the disk and ring currents for all the catalysts in the potential range of 0–0.8 V were found to be similar to those of commercial Pt/C. The Tafel plots in Fig. 7(c) describe the kinetics of the reaction. The slope values for $SrMn_{0.8}Fe_{0.2}O_3$, $SrMn_{0.7}Fe_{0.3}O_3$, $SrMn_{0.5}Fe_{0.5}O_3$ and Sr_2MnFeO_5 were 103 mV dec^{-1}, 105 mV dec^{-1}, 175 mV dec^{-1} and 88 mV dec^{-1}, respectively. These values, although higher than that of Pt/C, lie between 60 mV dec^{-1} and 120 mV dec^{-1} exhibiting faster kinetics. Based on the above results, it is evident that, among all the prepared samples, the $SrMn_{0.7}Fe_{0.3}O_3$ catalyst exhibits good ORR activity with a $4e^-$ dominated reaction pathway. Furthermore, the Nyquist plots in Fig. 7(d) show the charge transfer resistance (R_{ct}) of all the catalysts:

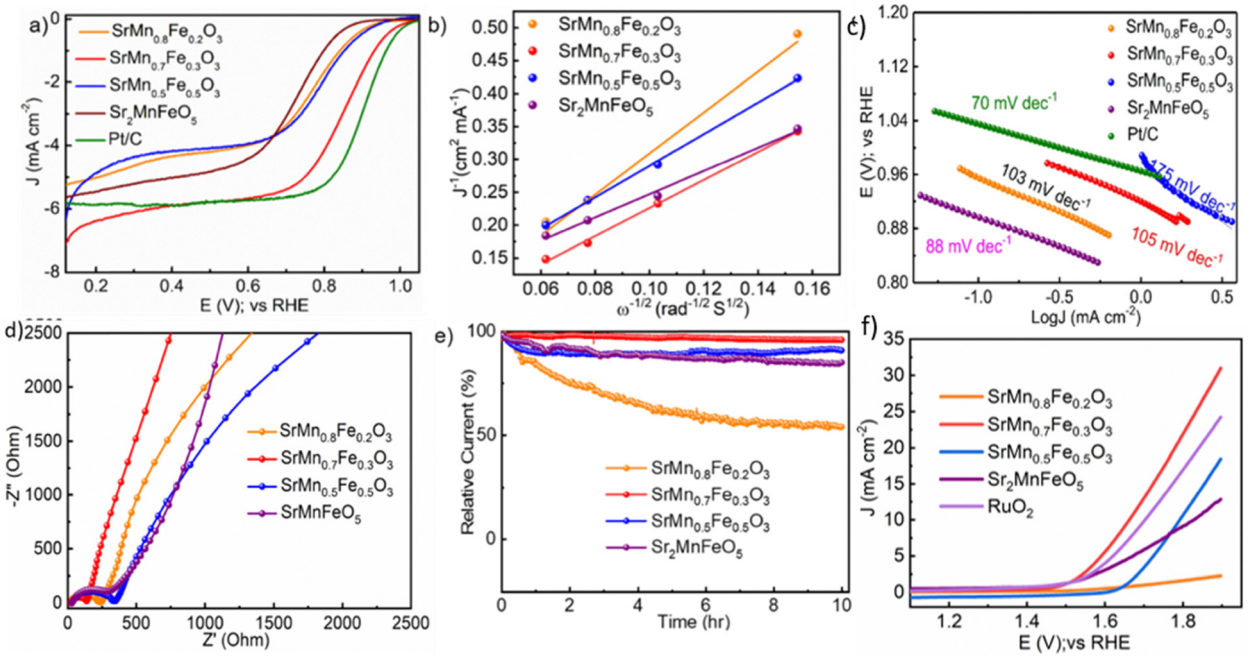

Fig. 7 (a) Comparative linear sweep voltammograms of all the catalysts including commercial Pt/C; (b) Koutecky–Levich plots; (c) Tafel plots; (d) Nyquist plots in O_2 medium; (e) chronoamperometric stability curves in 0.1 M KOH and (f) comparative OER linear sweep voltammograms in 0.1 M KOH under O_2 saturation at 1600 rpm for all the prepared compounds.

$SrMnO_3$ (226 Ω cm^{-2}), $SrMn_{0.8}Fe_{0.2}O_3$ (233 Ω cm^{-2}), $SrMn_{0.7}Fe_{0.3}O_3$ (136 Ω cm^{-2}), $SrMn_{0.5}Fe_{0.5}O_3$ (338 Ω cm^{-2}) and Sr_2MnFeO_5 (293 Ω cm^{-2}). Among them, $SrMn_{0.7}Fe_{0.3}O_3$ exhibits the lowest R_{ct}, thus indicating a high rate of electron transfer from the catalyst to the reactant in an oxygen environment, suggesting superior charge kinetics, which may further facilitate the ORR and OER kinetics. An equivalent circuit (Fig. S7, ESI†) has been modeled using the Randles circuit from the Nyquist plot. The Randles circuit provides information about both the faradaic region (solution resistance (R_s) and charge transfer resistance (R_{ct})) and the non-faradaic region (Q). Here, we represent a model with three elements: a resistor, a constant phase element (Q), and a Warburg diffusion element (W). The resistor comprises R_s and R_{ct}, while the Q describes the transportation of ions or electrons within the system. R_s and R_{ct} are connected in parallel to Q. The Warburg diffusion element is connected in series with the R_{ct}, thus providing insights into the diffusion of electroactive species between the surface of the electrode and electrolyte. Furthermore, the stability of all the doped catalysts was tested by chronoamperometry (Fig. 7(e)) in O_2-saturated 0.1 M KOH solution at a constant potential of 0.6 V (*vs.* RHE). $SrMn_{0.7}Fe_{0.3}O_3$ and $SrMn_{0.5}Fe_{0.5}O_3$ displayed excellent stability with 95.8% and 90.6% retention of the initial current densities after 10 hours, and Sr_2MnFeO_5 displayed good stability with an 85% retention and less degradation. $SrMn_{0.8}Fe_{0.2}O_3$ shows the least stability with a 54% retention of current density. Fig. S8 (ESI†) shows the stability of the Pt/C catalyst, which was tested by chronoamperometry in an O_2-saturated 0.1 M KOH solution at a constant potential of 0.6 V *vs.* RHE. The Pt/C catalyst retained 10% of its initial current density after 10 hours.

Besides, carbon-free perovskite oxides studied in previous literature, such as $La_{0.8}Sr_{0.2}MnO_3$,[56] $La_{0.5}Sr_{0.5}CoO_3$,[57] and $Ba_{0.5}Sr_{0.5}Co_{0.8}Fe_{0.2}O_3$,[58] were found to be very poor catalysts for the direct electroreduction of oxygen.[59] Consequently, they are usually used with a carbon additive. Carbon acts as a conductive agent and aids in the direct electroreduction of oxygen. In this report, we have studied intrinsically conducting perovskite oxides, focusing on the conductivity of materials that arises from their unique structural features, rather than from contributions by other materials or carbon, in relation to their ORR activity. Due to the conductive nature of the prepared perovskite oxides, obvious reduction peaks were observed in all the samples, indicating the reduction of oxygen molecules in the electrolyte. Fig. S11(a)–(h) (ESI†) presents the CV and LSV curves of all the catalysts with different rotations under similar conditions. Sr_2MnFeO_5 exhibits excellent ORR performance with an E_{onset} of 0.98 V and an $E_{1/2}$ of 0.82 V, comparable to those of commercial Pt/C, as shown in Table S5 (ESI†). Sr_2MnFeO_5 exhibits better ORR activity than the other two compositions, suggesting the optimized percentage of iron in the crystal and the deficiency of oxygen in the crystal system. With the optimal proportion of Fe, the ORR activity shows an enhancement, as shown clearly in Fig. 8(a). The K–L equation was used to determine the '*n*' of the catalysts, which shows a linear relationship and first-order kinetics (Fig. 8(b)). The measured '*n*' value of Sr_2MnFeO_5 at various potentials suggests that it adheres to a $4e^-$ oxygen reduction path. The R_{ct} values are found to be 318 Ω cm^{-2} for $SrMn_{0.8}Fe_{0.2}O_3$, 138 Ω cm^{-2} for $SrMn_{0.7}Fe_{0.3}O_3$, 175 Ω cm^{-2} for $SrMn_{0.5}Fe_{0.5}O_3$ and 132 Ω cm^{-2} for Sr_2MnFeO_5. $SrMn_{0.7}Fe_{0.3}O_5$ and Sr_2MnFeO_5 show the least R_{ct} among the catalysts as shown in Fig. 8(c).

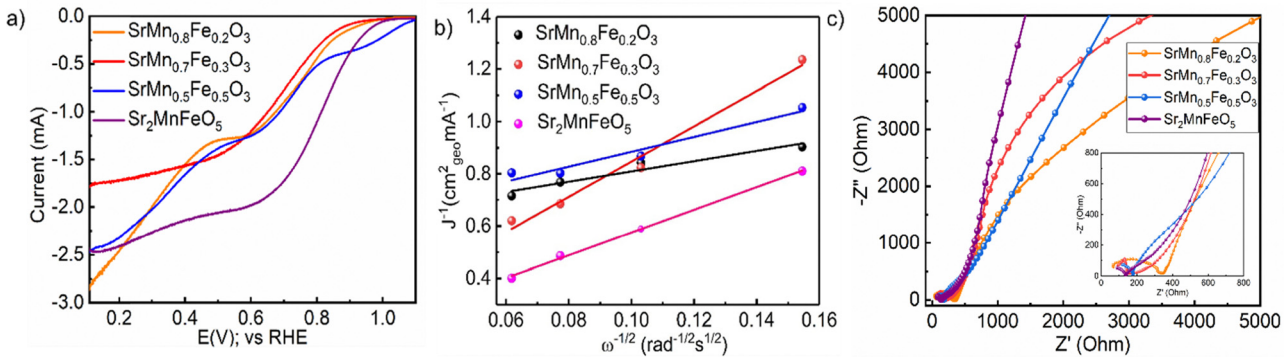

Fig. 8 (a) Comparative linear sweep voltammograms of all the catalysts without carbon (b) and their corresponding KL plots. (c) Impedance measurement of all the catalysts in O_2 saturated 0.1 M KOH.

To further check the bifunctionality of the catalysts, oxygen evolution measurements were carried out under the same environment with the RDE rotated at 1600 rpm, as shown in Fig. 7(f). The OER curve of $SrMn_{0.7}Fe_{0.3}O_3$ showed an onset potential of 1.5 V *vs.* RHE, with a current density of 30 mA cm^{-2}. The overpotential at 10 mA cm^{-2} was found to be 430 mV (compared to the theoretical value of 1.23 V). In contrast, the $SrMn_{0.5}Fe_{0.5}O_3$ sample exhibited an onset potential of 1.6 V, with an overpotential of 560 mV at 10 mA cm^{-2}. The remaining catalysts, $SrMn_{0.8}Fe_{0.2}O_3$ and Sr_2MnFeO_5, displayed the highest overpotentials, indicating very poor OER activity. $SrMn_{0.7}Fe_{0.3}O_3$ and $SrMn_{0.5}Fe_{0.5}O_3$ demonstrated superior OER electrocatalytic activity, with the highest current densities. Furthermore, the stability of the doped catalysts was evaluated by chronoamperometry after the OER in an O_2-saturated 0.1 M KOH solution at a constant potential of 0.6 V *vs.* RHE (Fig. S9, ESI†). $SrMn_{0.7}Fe_{0.3}O_3$ and $SrMn_{0.5}Fe_{0.5}O_3$ exhibited excellent stability, retaining 99% and 97% of their initial current densities after 10 hours, respectively. The ECSA-normalized current density (j_{ECSA}) is a crucial parameter indicating the intrinsic activity of a catalyst. It can be estimated from the electric double-layer capacitance (C_{dl}, Fig. S14, ESI†), obtained from a non-faradaic CV curve (Fig. S13, ESI†). As shown by the ECSA-normalized current curves (Fig. S10, ESI†), $SrMn_{0.7}Fe_{0.3}O_3$ exhibited the lowest overpotential at 0.5 mA cm^{-2} ECSA, indicating that it is the most active catalyst, followed by $SrMnFeO_5$, $SrMn_{0.8}Fe_{0.2}O_3$, and $SrMn_{0.5}Fe_{0.5}O_3$. TOF is used to measure the number of active sites on the catalyst and was calculated using the formula given in eqn (8). The TOF values obtained are as follows: 0.82 s^{-1} for $SrMn_{0.8}Fe_{0.2}O_3$, 11.12 s^{-1} for $SrMn_{0.7}Fe_{0.3}O_3$, 6.59 s^{-1} for $SrMn_{0.5}Fe_{0.5}O_3$, and 3.14 s^{-1} for Sr_2MnFeO_5. This enhanced performance is attributed to the partial substitution of Mn by Fe at the B site, where the presence of redox-active Mn^{3+}/Mn^{4+} and Fe^{3+}/Fe^{2+} ions in the structure promotes superior electrocatalytic activity in $SrMn_{0.7}Fe_{0.3}O_3$. In the OER studies performed on all catalysts without carbon, none of the catalysts reached a current density of 10 mA cm^{-2}, as shown in Fig. S11(i) (ESI†). To further assess the robustness of the material, the $SrMn_{0.7}Fe_{0.3}O_3$ catalyst was cycled for 30 000 cycles. Post-cycling stability characterization was performed using XRD and SEM, with the results presented in Fig. S12(a)–(d) (ESI†). The XRD results show that fewer peaks were retained, and the remaining peaks shifted to lower angles. The SEM images reveal that while the morphology was generally retained, an increase in particle size was observed. The corresponding EDS analysis confirms the elemental composition, but the peak intensities are weak due to the dominance of the carbon substrate. Overall, the post-stability changes observed in the XRD, SEM, and EDS results could be attributed to lattice expansion or phase transitions induced by the electrochemical conditions, including interactions with the electrolyte, the applied potential, or the effect of the carbon paper substrate on the catalyst layer.

Furthermore, the intrinsic electrocatalytic performance of all the catalysts can be correlated with the crystal structural arrangement, bond length, electronic properties and the various activity metrics like ECSA, mass activity and specific activity. $SrMnO_3$ crystallised as 4-hexagonal perovskite oxide (Fig. 2(a)). The structure is modified by doping with transition-metal ions (Fe) at the B site of $SrMnO_3$; however, the Fe ion as a dopant causes the structural changes from hexagonal to trigonal Fig. 2(b)–(d). When an excess proportion of the dopant Fe is substituted at the Mn site, oxygen vacancies are generated and the structure changes to orthorhombic. The simple perovskite oxide $SrMnO_3$ possesses a hexagonal system and the substituted B site variants ($SrMn_{1-x}Fe_xO_3$, where x = 0.2, 0.3, 0.5) $SrMn_{0.8}Fe_{0.2}O_3$, $SrMn_{0.7}Fe_{0.3}O_3$, and $SrMn_{0.5}Fe_{0.5}O_3$ possess a trigonal crystal system. Fig. S15(a) and (b) (ESI†) depicts the distribution of atoms in isotropic distribution. When Fe and Mn are in equal proportion at the B site (Fe = 1 and Mn = 1), the resulting oxygen-deficient perovskite oxide Sr_2MnFeO_5 possesses an orthorhombic structure. The phase transition from hexagonal to trigonal in $SrMnO_3$ occurs when an element with a different ionic radius is substituted at the B site, causing non-stoichiometric changes. Hence, the metal ions move towards face-sharing octahedra, forming a trigonal structure as the percentage of iron increases. Furthermore, the structure changes to orthorhombic, and the composition changes to a brownmillerite phase, *i.e.*, Sr_2MnFeO_5. Brownmillerite is an oxygen-deficient structure forming zigzag chains of alternating layers of [Mn/FeO_6] octahedra and [Mn/FeO_4] tetrahedra, as shown in Fig. 2(e) and Fig. S15(c) (ESI†), which could offer

a pathway for the transport of oxygen ions with higher mobility. The oxygen-deficient tetrahedra exhibit an anisotropic distribution, suggesting that brownmillerite has lower kinetic activity. This kinetic barrier is due to the zigzag motion of ion transport, which results in a slower reaction rate and, consequently, a decrease in current density. In contrast, for catalysts with an isotropic distribution, the kinetic barrier is lower because ion transport is faster, and the presence of carbon enhances the catalyst's activity, leading to an increase in current density. According to Sabatier's principle, the binding affinity of the catalyst to the intermediates should not be too strong or too weak. The e_g orbital electron filling is one of the descriptors predicting the binding affinity of the catalyst. The average number of e_g electrons for $SrMn_{0.7}Fe_{0.3}O_3$ was found to be 1.12, and for Sr_2MnFeO_5, it was unity (see S19, ESI†). Another important criterion for the assessment of catalytic activity is the Mn–O and Fe–O bond lengths and Mn–O–Fe angle. The bond lengths and bond angles were calculated after refinement, and bond valence sum (BVS) analysis was performed for all the catalysts, as listed in Tables S6 and S7 (ESI†). $SrMn_{0.7}Fe_{0.3}O_3$ shows a longer bond length compared to the other catalysts, which enables feasible interactions between the surfaces and adsorbed intermediates, thus enhancing diffusion kinetics. A longer bond length results in a weaker binding strength, facilitating the easier release of intermediates and enabling the catalytic reactions to proceed more efficiently. Since the intermediates are not strongly bound to the surface, they can readily participate in further reactions. A longer bond between the catalyst surface and the adsorbed intermediate requires less energy for desorption, speeding up the reaction step. Optimized adsorption energy, achieved by a moderate bond length, enables an optimal interaction between the catalyst and the reactant molecules, promoting efficient catalysis. An important step in assessing the intrinsic activity metrics of a catalyst is determining the available catalytic active sites for the reaction. The ECSA, mass activity, and specific activity of all the catalysts are listed in Table S8 (ESI†). $SrMn_{0.7}Fe_{0.3}O_3$ displays the highest ECSA, mass activity, and specific activity, as shown in Fig. S17 and S18 (ESI†). Moreover, the bifunctionality index is another crucial descriptor for evaluating catalytic performance as shown in Fig. S16 (ESI†). This index is calculated using the relation: $\Delta E = E_{j-10} - E_{1/2}$, where E_{j-10} is the OER potential at a current density of 10 mA cm^{-2} and $E_{1/2}$ is the half-wave potential obtained from the ORR polarization curve, which is 0.82 V for $SrMn_{0.7}Fe_{0.3}O_3$. A smaller ΔE value indicates a better bifunctional performance of the catalyst. Finally, all the intrinsic descriptors applied in the bifunctional mechanism, illustrating the four-electron pathway for both the ORR and OER, with carbon driving the reaction externally, are shown in Fig. S17 (ESI†). These results correlate with the XRD, BVS calculation, and e_g calculations. Additionally, the ORR mechanism for the intrinsically conducting brownmillerite Sr_2MnFeO_5 without carbon is further explored in Fig. S18 (ESI†).

Fig. 9(a) illustrates the polarization and power density curves of ZABs comprising $SrMn_{0.7}Fe_{0.3}O_3$ and $SrMn_{0.5}Fe_{0.5}O_3$ cathode catalysts wherein both catalysts demonstrate a voltage of 1.4 V

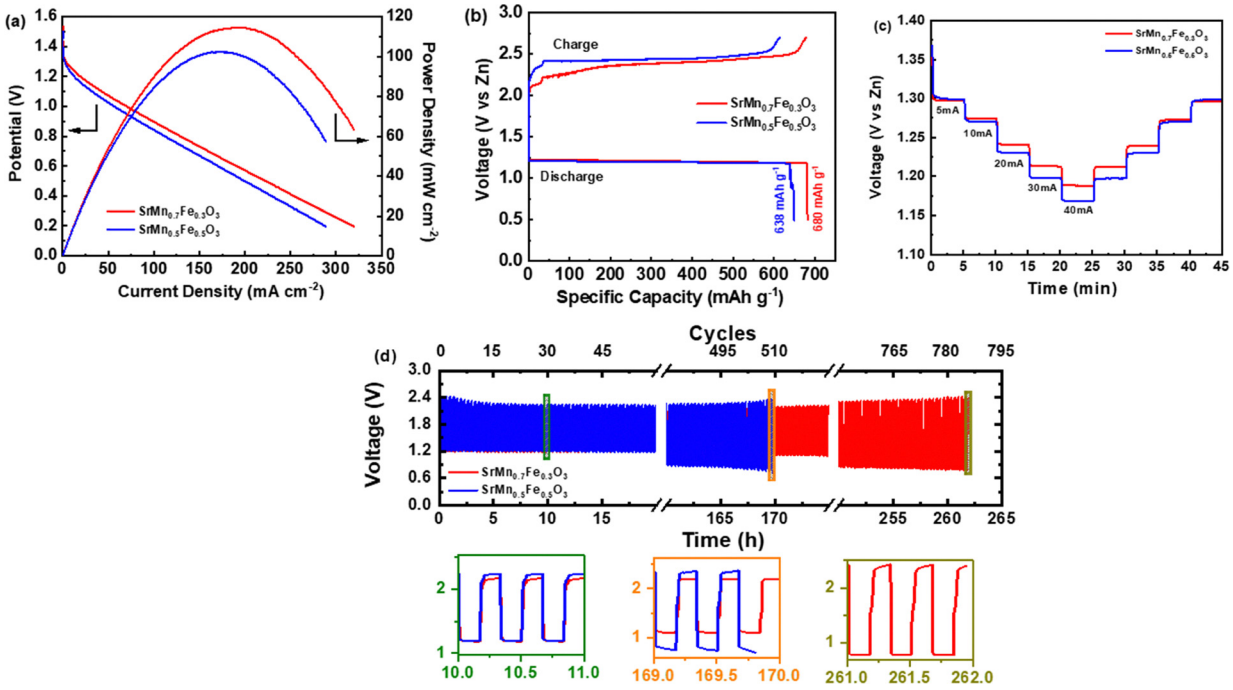

Fig. 9 Assessment of the ZAB performance with $SrMn_{0.7}Fe_{0.3}O_3$ and $SrMn_{0.5}Fe_{0.5}O_3$ catalysts under full-cell configuration: (a) polarization (*I*–*V*) curve trends and associated power densities. (b) Charge–discharge profiles showing specific capacities of 680 and 638 mA h g^{-1} for $SrMn_{0.7}Fe_{0.3}O_3$ and $SrMn_{0.5}Fe_{0.5}O_3$, respectively. (c) Rate capability test at different current rates, ranging from low current (5 mA) to high current (40 mA), for $SrMn_{0.7}Fe_{0.3}O_3$ and $SrMn_{0.5}Fe_{0.5}O_3$. (d) The galvanostatic charge–discharge graphical profiles of ZABs incorporating $SrMn_{0.7}Fe_{0.3}O_3$ and $SrMn_{0.5}Fe_{0.5}O_3$ catalysts at 5 mA cm^{-2}.

in an open circuit scenario. With an increase in current density, the ZAB comprising the $SrMn_{0.7}Fe_{0.3}O_3$ catalyst shows superior performance when compared to other catalysts. The $SrMn_{0.7}Fe_{0.3}O_3$ catalyst exhibits a peak power density of 114 mW cm^{-2} at a 200 mA cm^{-2} current density, while the $SrMn_{0.5}Fe_{0.5}O_3$ catalyst reaches a peak power density of 102 mW cm^{-2} at a current density of 172 mA cm^{-2}. Fig. 9(b) shows the galvanostatic discharge results of the $SrMn_{0.7}Fe_{0.3}O_3$ and $SrMn_{0.5}Fe_{0.5}O_3$ catalysts. The $SrMn_{0.7}Fe_{0.3}O_3$ catalyst exhibits a specific capacity of 680 mA h g^{-1}, whereas the $SrMn_{0.5}Fe_{0.5}O_3$ catalyst shows a specific capacity of 638 mA h g^{-1}. The relatively high specific capacities of these catalysts reflect their substantial energy storage capabilities. The rate capability of the $SrMn_{0.7}Fe_{0.3}O_3$ and $SrMn_{0.5}Fe_{0.5}O_3$ catalysts is evaluated at varying current densities ranging from 5 to 40 mA cm^{-2}, as illustrated in Fig. 9(c). The electrodes displayed small variations in constant current discharge measurements. As the rate of discharge current increased, the discharge potential plateau shifted downward due to low ORR kinetics. However, the voltage plateau remained consistent during step-down from high to low current and step-up from low to high current, indicating greater mass transfer efficacy and better electrocatalytic activity. When the current density dropped to 5 mA cm^{-2}, the discharge recovered completely, confirming good reversibility.

Fig. 9(d) illustrates the long-term performance and efficiency of ZABs with $SrMn_{0.7}Fe_{0.3}O_3$ and $SrMn_{0.5}Fe_{0.5}O_3$ catalysts as air cathode catalysts, evaluated through galvanostatic charge–discharge cycling conducted at room temperature and at a current density of 5 mA cm^{-2}. Initially, both batteries showed a discharge voltage of 1.18 V and a charge voltage of 2.04 V, resulting in a voltage gap (ΔE) of 0.86 V and an initial round-trip efficiency of 58%. As the number of cycles increased, both the voltage gap including round-trip efficacy deteriorated. After 170 hours of continuous cycling (510 cycles), the $SrMn_{0.7}Fe_{0.3}O_3$-based battery shows a rise in voltage gap to 1.07 V and a decrease in round-trip efficiency to 50.4%. In contrast, the $SrMn_{0.5}Fe_{0.5}O_3$-based battery experienced a more substantial increase in voltage gap to 1.56 V and a significant drop in round-trip efficiency to 32%. After 262 hours of continuous cycling (786 cycles), the $SrMn_{0.7}Fe_{0.3}O_3$-based battery showed a further increase in voltage gap to 1.51 V and a decrease in round-trip efficiency to 34%. These results indicate that $SrMn_{0.7}Fe_{0.3}O_3$ maintains better initial performance and greater stability over long-term cycling compared to $SrMn_{0.5}Fe_{0.5}O_3$. The superior performance of $SrMn_{0.7}Fe_{0.3}O_3$ suggests that it is a more reliable and efficient choice for applications requiring extended battery life and stability.

This research effectively assessed the performance of ZABs using $SrMn_{0.7}Fe_{0.3}O_3$ and $SrMn_{0.5}Fe_{0.5}O_3$ as air cathode catalysts. ZABs with $SrMn_{0.7}Fe_{0.3}O_3$ as the cathode catalyst exhibits higher specific capacity, peak power density, and stability, offering promise for advanced energy storage solutions.

4. Conclusions

In conclusion, we synthesized a series of $SrMn_{1-x}Fe_xO_3$ (x = 0.2, 0.3, 0.5) and Sr_2MnFeO_5 perovskite oxides by the molten salt synthesis method, substituting iron at the manganese site. The synthesized catalysts were thoroughly characterized, and their structural properties were assessed, revealing phase and composition transitions with increasing doping percentages. Compared to simple perovskite oxides, the iron-substituted variants exhibited significantly enhanced catalytic activity. The best performing catalyst, $SrMn_{0.7}Fe_{0.3}O_3$, exhibited an onset potential of 0.99 V and 1.6 V *vs.* RHE for the ORR and OER, respectively, comparable to those of precious metal catalysts. This confirms that changes in the crystal structure enhance the conductivity of perovskite oxides, contributing to their superior performance. Furthermore, among all perovskite oxides examined without carbon support, a brownmillerite, Sr_2MnFeO_5, achieved an onset potential of 0.97 V *vs.* RHE, demonstrating the highest catalytic activity *via* a four-electron transfer route that mitigates mass transport issues. Additionally, a ZAB unit with catalysts $SrMn_{0.7}Fe_{0.3}O_3$ and $SrMn_{0.5}Fe_{0.5}O_3$ was developed, resulting in a high overall efficiency for $SrMn_{0.7}Fe_{0.3}O_3$. This device provides a power density of 114 mW cm^{-2}, a high specific capacity of 680 mA h g^{-1}, and a steady operation for more than 786 cycles over 262 hours. This study opens new avenues for developing efficient electrocatalysts based on perovskite oxides by leveraging structural modifications to enhance electronic properties and catalytic performance.

Data availability

The data supporting this article have been included as part of the ESI.†

Conflicts of interest

The authors declare no conflicts of interests.

Acknowledgements

This work was supported financially by the Department of Science and Technology, DST SERB Core Research Grant (CRG) (ref. no. CRG/2019/003696). The authors also acknowledge the financial support from DST-FIST (Fund for the Improvement of S&T Infrastructure) to the Department of Chemistry, SRM Institute of Science and Technology, under grant no. SR/FST/CST-266/2015(c).

References

1 Y. Wang, X. Yang, C. Hou, F. Yin, G. Wang, X. Zhu, G. Jiang and C. Li, Improved Catalytic Activity and Stability of Ba Substituted $SrTiO_3$ Perovskite for Oxidative Coupling of Methane, *ChemCatChem*, 2021, **13**(19), 4182–4191, DOI: 10.1002/cctc.202100859.

2 W. Haizhen, M. Zhou, P. Choudhury and H. Luo, Perovskite oxides as bifunctional oxygen electrocatalysts for oxygen evolution/reduction reactions–A mini review, *Appl. Mater. Today*, 2019, **16**, 56–71, DOI: 10.1016/j.apmt.2019.05.004.

3 H. Xiubing, G. Zhao, G. Wang and J. T. S. Irvine, Advances in porous perovskites: synthesis and electrocatalytic performance in fuel cells and metal–air batteries, *Energy Environ. Mater. Chem. Sci.*, 2018, **9**(15), 3623–3637, DOI: 10.1039/C7SC03920D.
4 Y. Jie, R. Ran, Y. Zhong, W. Zhou, M. Ni and Z. Shao, Recent advances in oxygen electrocatalysts based on perovskite oxides, *Energy Environ. Sci.*, 2020, **3**, 121–145, DOI: 10.1002/eem2.12064.
5 X. Jun, C. Chen, Z. Han, Y. Yang, J. Li and Q. Deng, Recent advances in oxygen electrocatalysts based on perovskite oxides, *Nanomaterials*, 2019, **9**(8), 1161, DOI: 10.3390/nano9081161.
6 H. Jonathan, Z. Feng, N. Charles, X. Renshaw Wang, D. Lee, K. A. Stoerzinger and S. Muy, Tuning perovskite oxides by strain: Electronic structure, properties, and functions in (electro) catalysis andferroelectricity, *Mater. Today*, 2019, **31**, 100–118, DOI: 10.1016/j.mattod.2019.03.014.
7 W. Yao, D. Wang and Y. Li, A fundamental comprehension and recent progress in advanced Pt-based ORR nanocatalysts, *Smart Mater.*, 2021, **2**(1), 56–75, DOI: 10.1002/smm2.1023.
8 S. Yiling, X. Zhang, X. Cui and J. Shi, The ORR kinetics of ZIF-derived FeNC electrocatalysts, *J. Catal.*, 2019, **372**, 174–181, DOI: 10.1016/j.jcat.2019.02.023.
9 S. Meng, H. Liu, Y. Liu, J. Qu and J. Li, Graphene-based transition metal oxide nanocomposites for the oxygen reduction reaction, *Nanoscale*, 2015, **7**(4), 1250–1269, DOI: 10.1039/C4NR05838K.
10 L. Bo-Quan, C. X. Zhao, J. N. Liu and Q. Zhang, Electrosynthesis of hydrogen peroxide synergistically catalyzed by atomic Co–N_x–C sites and oxygen functional groups in noble-metal-free electrocatalysts, *Adv. Mater.*, 2019, **31**(35), 1808173, DOI: 10.1002/adma.201808173.
11 Z. Shenlong, H. Y. Du, L. He, K. Zhao, L. Chang, G. Yin, H. Zhao, S. Liu and Z. Tang, Carbonized nanoscale metal–organic frameworks as high performance electrocatalyst for oxygen reduction reaction, *ACS Nano*, 2014, **8**(12), 12660–12668, DOI: 10.1021/nn505582e.
12 Y. Xingwen and S. Ye, Recent advances in activity and durability enhancement of Pt/C catalytic cathode in PEMFC: Part I. Physico-chemical and electronic interaction between Pt and carbon support, and activity enhancement of Pt/C catalyst, *J. Power Sources*, 2007, **172**(1), 133–144, DOI: 10.1016/j.jpowsour.2007.07.049.
13 B. Gaetan, M. J. Eslamibidgoli, A. H. Youssef, S. Garbarino, A. Ruediger, M. Eikerling and D. Guay, Effect of IrO_6 octahedron distortion on the OER activity at (100) IrO_2 thin film, *ACS Catal.*, 2019, **10**(1), 806–817, DOI: 10.1021/acscatal.9b04347.
14 W. Cheng, L. Jin, H. Shang, H. Xu, Y. Shiraishi and Y. Du, Advances in engineering RuO_2 electrocatalysts towards oxygen evolution reaction, *Chin. Chem. Lett.*, 2021, **32**(7), 2108–2116, DOI: 10.1016/j.cclet.2020.11.051.
15 Z. Jian, Q. Zhang and X. Feng, Support and interface effects in water-splitting electrocatalysts., *Adv. Mater.*, 2019, **31**, 1808167, DOI: 10.1002/adma.201808167.
16 S. Qiurong, C. Zhu, D. Du and Y. Lin, Robust noble metal-based electrocatalysts for oxygen evolution reaction., *Chem. Soc. Rev.*, 2019, **48**(12), 3181–3192, DOI: 10.1039/C8CS00671G.
17 G. Chiranjita, K. K. Hazarika and P. Bharali, Transition metal oxide nanocatalysts for oxygen reduction reaction, *Mater. Sci. Energy Techol.*, 2018, **1**(2), 117–128.
18 P. Puerto, A. Kai Ling Ng, K. Fahy, A. E. Goode, M. P. Ryan and A. Kucernak, Supported transition metal phosphides: activity survey for HER, ORR, OER, and corrosion resistance in acid and alkaline electrolytes, *ACS Catal.*, 2019, **9**(12), 11515–11529, DOI: 10.1021/acscatal.9b03359.
19 Z. Yunmin, X. Liu, S. Jin, H. Chen, W. Lee, M. Liu and Y. Chen, Anionic defect engineering of transition metal oxides for oxygen reduction and evolution reactions, *J. Mater. Chem. A*, 2019, **7**(11), 5875–5897, DOI: 10.1039/C8TA12477A.
20 B. Antoine, A. S. Ryabova, T. Schott, G. Kéranguéven, S. Istomin, E. V. Antipov and E. R. Savinova, Challenges in the understanding oxygen reduction electrocatalysis on transition metal oxides., *Curr. Opin. Electrochem.*, 2019, **14**, 23–31, DOI: 10.1016/j.coelec.2018.09.010.
21 D. Chandni, N. Sinha and P. Roy, Transition Metal Non-Oxides as Electrocatalysts: Advantages and Challenges, *Small*, 2022, **18**(28), 2202033, DOI: 10.1002/smll.202202033.
22 X. Yejian, S. Sun, Q. Wang, Z. Dong and Z. Liu, Transition metal oxide-based oxygen reduction reaction electrocatalysts for energy conversion systems with aqueous electrolytes, *J. Mater. Chem. A*, 2018, **6**(23), 10595–10626, DOI: 10.1039/C7TA10569J.
23 X. Wei, H. Yin, T. Wu and H. Li, Challenges and Opportunities of Transition Metal Oxides as Electrocatalysts., *Chem. – Eur. J.*, 2023, **29**(5), e202202872, DOI: 10.1002/chem.202202872.
24 A. Daniel Adjei, Y. Zheng, T. H. Lee, M. Park, W. Tamakloe, G. H. Lee, H. W. Jang, K. Cho and Y. M. Kang, Synergistic catalysis of the lattice oxygen and transition Metal facilitating ORR and OER in perovskite catalysts for Li–O_2 batteries., *ACS Catal.*, 2020, **11**(1), 424–434, DOI: 10.1021/acscatal.0c02608.
25 W. Chao, Z. Feng, G. G. Scherer, J. Barber, Y. S. Horn and Z. J. Xu, Cations in octahedral sites: a descriptor for oxygen electrocatalysis on transition-metal spinels., *Adv. Mater.*, 2017, **29**(23), 1606800, DOI: 10.1039/D3QM00841J.
26 E. Rios, J.-L. Gautier, G. Poillerat and P. Chartier, Mixed valency spinel oxides of transition metals and electrocatalysis: case of the $MnxCo_{3-x}O_4$ system, *Electrochim. Acta*, 1998, **44**(8–9), 1491–1497, DOI: 10.1016/S0013-4686(98)00272-2.
27 H. B. Parse, I. Patil, B. Kakade and A. Swami, Cobalt Nanoparticles Encapsulated in N-Doped Carbon on the Surface of MXene (Ti_3C_2) Play a Key Role for Electroreduction of Oxygen, *Energy Fuels*, 2021, **35**(21), 17909–17918, DOI: 10.1021/acs.energyfuels.1c02486.
28 M. Retuerto, A. González Pereira, F. J. Pérez-Alonso, M. A. Peña, J. Luis, G. Fierro, J. A. Alonso, M. T. Fernández-Díaz, L. Pascual and S. Rojas, Structural effects of $LaNiO_3$ as

electrocatalyst for the oxygen reduction reaction, *Appl. Catal., B*, 2017, **203**, 363–371, DOI: 10.1016/j.apcatb.2016.10.016.

29 R. Zhao, Q. Li, X. Jiang, S. Huang, G. Fu and J. Lee, Interface engineering in transition metal-based heterostructures for oxygen electrocatalysis, *Mater. Chem. Front.*, 2021, **5**(3), 1033–1059, DOI: 10.1039/D0QM00729C.

30 S. Zongping, W. Yang, Y. Cong, H. Dong, J. Tong and G. Xiong., Investigation of the permeation behavior and stability of a $Ba_{0.5}Sr_{0.5}Co_{0.8}Fe_{0.2}O_{3-\delta}$ oxygen membrane, *J. Membr. Sci.*, 2000, **172**(1–2), 177–188, DOI: 10.1016/S0376-7388(00)00337-9.

31 N. Kumar, M. Kumar, T. C. Nagaiah, V. Siruguri, S. Rayaprol, A. K. Yadav, S. N. Jha, D. Bhattacharyya and A. Kumar Paul, Investigation of new B-site-disordered perovskite oxide $CaLaScRuO_{6+\delta}$: an efficient oxygen bifunctional electrocatalyst in a highly alkaline medium, *ACS Appl. Mater. Interfaces*, 2020, **12**(8), 9190–9200, DOI: 10.1021/acsami.9b20199.

32 J. Sun, L. Du, B. Sun, G. Han, Y. Ma, J. Wang, H. Huo, C. Du and G. Yin, Bifunctional $LaMn_{0.3}Co_{0.7}O_3$ perovskite oxide catalyst for oxygen reduction and evolution reactions: the optimized eg electronic structures by manganese dopant, *ACS Appl. Mater. Interfaces*, 2020, **12**(22), 24717–24725, DOI: 10.1021/acsami.0c03983.

33 Y. Jiang, Z. Geng, Y. Sun, X. Wang, K. Huang, Y. Cong, F. Shi, Y. Wang, W. Zhang and S. Feng, Highly efficient B-site exsolution assisted by Co doping in lanthanum ferrite toward high-performance electrocatalysts for oxygen evolution and oxygen reduction, *ACS Sustainable Chem. Eng.*, 2019, **8**(1–9), 302–310, DOI: 10.1021/acssuschemeng.9b05344.

34 R. A. Eichel, Structural and dynamic properties of oxygen vacancies in perovskite oxides—analysis of defect chemistry by modern multi-frequency and pulsed EPR techniques, *Phys. Chem. Chem. Phys.*, 2011, **13**, 368–384, DOI: 10.1039/B918782K.

35 J. Yang, S. Hu, Y. Fang, S. Hoang, L. Li, W. Yang and Z. Liang, Oxygen vacancy promoted O_2 activation over perovskite oxide for low-temperature CO oxidation, *ACS Catal.*, 2019, **9**(11), 9751–9763, DOI: 10.1021/acscatal.9b02408.

36 C. F. Chen, G. King, R. M. Dickerson, P. A. Papin, S. Gupta, W. R. Kellogg and G. Wu, Oxygen-deficient $BaTiO_{3-x}$ perovskite as an efficient bifunctional oxygen electrocatalyst, *Nano Energy*, 2015, **13**, 423–432, DOI: 10.1016/j.nanoen.2015.03.005.

37 H. Miao, X. Wu, B. Chen, Q. Wang, F. Wang, J. Wang, C. Zhang, H. Zhang, J. Yuan and Q. Zhang, A-site deficient/excessive effects of $LaMnO_3$ perovskite as bifunctional oxygen catalyst for zinc–air batteries, *Electrochim. Acta*, 2020, **333**, 135566, DOI: 10.1016/j.electacta.2019.135566.

38 R. Xie, Z. Nie, X. Hu, Y. Yu, C. Aruta and N. Yang, Pr-doped $LaCoO_3$ toward stable and efficient oxygen evolution reaction, *ACS Appl. Energy Mater.*, 2021, **4**, 9057–9065, DOI: 10.1021/acsaem.1c01348.

39 X. Song, S. Le, X. Zhu, L. Qin, Y. Luo, Y. Li, K. Sun and Y. Chen, High performance $BaFe_{1-x}Bi_xO_{3-\delta}$ as cobalt-free cathodes for intermediate temperature solid oxide fuel cells, *Int J. Hydrogen Energy*, 2017, **42**(24), 15808–15817, DOI: 10.1016/j.ijhydene.2017.05.061.

40 F. Dong, M. Ni, W. He, Y. Chen, G. Yang, D. Chen and Z. Shao, An efficient electrocatalyst as cathode material for solid oxide fuel cells: $BaFe_{0.9}Sn_{0.05}O_{3-\delta}$, *J. Power Sources*, 2016, **326**, 459–465, DOI: 10.1016/j.jpowsour.2016.07.023.

41 M. Elhousseini, S. Berk Şanlı, S. Dekyvere, G. Ç. Hussein, A. Younus, F. Pişkin, F. Verpoort and B. Pişkin, A dual-doping strategy of $LaCoO_3$ for optimized oxygen evolution reaction toward zinc–air batteries application, *Int. J. Energy Res.*, 2022, **46**(15), 22014–22024, DOI: 10.1002/er.8719.

42 E. Tsuji, T. Motohashi, H. Noda, Y. Aoki and H. Habazaki, Strong lanthanoid substitution effect on electrocatalytic activity of double-perovskite-type $BaLnMn_2O_5$ (Ln = Y, Gd, Nd, and La) for oxygen reduction reaction, *J. Phys. Chem. C*, 2018, **122**(13), 7081–7087, DOI: 10.1021/acs.jpcc.7b12678.

43 J. Xingdong, Y. Dong, Z. Zhang, J. Li, J. Qian and D. Gao., Cation substitution of B-site in $LaCoO_3$ for bifunctional oxygen electrocatalytic activities, *J. Alloys Compd.*, 2021, **878**, 160433, DOI: 10.1016/j.jallcom.2021.160433.

44 Z. Zhuang, Y. Li, R. Yu, L. Xia, J. Yang, Z. Lang and J. Zhu, Reversely trapping atoms from a perovskite surface for high-performance and durable fuel cell cathodes, *Nat. Catal.*, 2022, **5**(4), 300–310, DOI: 10.1038/s41929-024-01214-4.

45 M. Islam, M. G. Jeong, I. H. Oh, K. W. Nam and H. G. Jung, Role of strontium as doping agent in $LaMn_{0.5}Ni_{0.5}O_3$ for oxygen electro-catalysis, *J. Ind. Eng. Chem.*, 2020, **85**, 94–101, DOI: 10.1016/j.jiec.2020.01.026.

46 J. Haoqing, M. Wang, S. Liu, H. Sun, J. Liu, Z. Hou, T. Qian and C. Yan, Identifying the Lewis base chemistry in preventing the deposition of metal oxides on ketone-enriched carbon cathodes for highly durable metal–air batteries, *ACS Appl. Mater.*, 2019, **12**(3), 3603–3609, DOI: 10.1021/acsami.9b18651.

47 W. Mengfan, S. Liu, N. Xu, T. Qian and C. Yan, Active Fe–N_x sites in carbon nanosheets as oxygen reduction electrocatalyst for flexible all-solid-state zinc–air batteries, *Adv. Sustainable Syst.*, 2017, **1**(10), 1700085, DOI: 10.1002/adsu.201700085.

48 Z. Yinlong, H. A. Tahini, Z. Hu, Z.-G. Chen, W. Zhou, A. C. Komarek and Q. Lin, *et al.*, Boosting oxygen evolution reaction by creating both metal ion and lattice-oxygen active sites in a complex oxide, *Adv. Mater.*, 2020, **32**(1), 1905025, DOI: 10.1002/adma.201905025.

49 X. Zhongyuan, B. Deng, Y. Wang, Z. Jiang and Z.-J. Jiang., Synergistic co-doping induced high catalytic activities of La/Fe doped Co_3O_4 towards oxygen reduction/evolution reactions for Zn–air batteries, *J. Mater. Chem. A*, 2022, **10**(44), 23483–23493, DOI: 10.1039/D2TA06726A.

50 C. M. Enoch, S. Ingavale, P. Marbaniang, I. Patil and A. Swami, Molten Salt-Directed Synthesis of Strontium Manganese Perovskite Oxide: An Active Electro-Catalyst for Oxygen Reduction Reaction and Oxygen Evolution Reaction., *J. Mater. Chem. A*, 2023, **11**, 21780–21792, DOI: 10.1039/D3TA03808D.

51 I. M. Patil, A. Swami, R. Chavan, M. Lokanathan and B. Kakade, Hexagonal boron nitride-supported crystalline manganese oxide nanorods/carbon: a tunable nanocomposite catalyst for dioxygen electroreduction, *ACS Sustainable Chem. Eng.*, 2018, **12**(6), 16886–16895, DOI: **10.1021/acssuschemeng.8b04241**.

52 I. patil, M. Lokanathan, B. Ganesan, A. Swami and B. Kakade, Carbon nanotube/boron nitride nanocomposite as a significant bifunctional electrocatalyst for oxygen reduction and oxygen evolution reactions, *Chem. – Eur. J.*, 2017, **23**(3), 676–683, DOI: **10.1002/chem.201604231**.

53 S. Jia, L. Du, B. Sun, G. Han, Y. Ma, J. Wang, H. Huo, C. Du and G. Yin, Bifunctional $LaMn_{0.3}Co_{0.7}O_3$ perovskite oxide catalyst for oxygen reduction and evolution reactions: the optimized eg electronic structures by manganese dopant, *ACS Appl. Mater. Interfaces*, 2020, **22**, 24717–24725, DOI: **10.1021/acsami.0c03983**.

54 P. Varathan, S. K. Das and A. K. Sahu, Nanoarchitecture of 2D materials: unveiling the power trio-Ni, Co and GNF-in eco-friendly air breating zinc air battey through layered double hydroxides, *J. Energy Storage*, 2024, **90**, 111845, DOI: **10.1016/j.est.2024.111845**.

55 P. Varathan, P. Moni, S. K. Das and A. K. Sahu, High performance air breathing Zinc–Air batterry with Pt–Ni and Pt–Co bifunctional electrocatalyst on N activated mesoporous carbon, *J. Electrochem. Soc.*, 2023, **170**(5), 050536, DOI: **10.1149/1945-7111/acd352**.

56 Y. Litao, Y. Lin, X. Yu, W. Xu, T. Salas, H. Smallidge, M. Zhou and H. Luo, $La_{0.8}Sr_{0.2}MnO_3$-based perovskite nanoparticles with the A-site deficiency as high performance bifunctional oxygen catalyst in alkaline solution, *ACS Appl. Mater. Interfaces*, 2017, **9**(28), 23820–23827, DOI: **10.1021/acsami.7b06458**.

57 B. Casey, E. Fabbri, A. H. Clark, N. S. Yüzbasi, T. Graule and T. J. Schmidt, Influence of carbon on the dynamic changes in Co oxidation state of $Ba_{0.5}Sr_{0.5}Co_{0.8}Fe_{0.2}O_{3-\delta}$ perovskite catalyst during the oxygen reduction and evolution reactions, *EcoMat.*, 2023, 12353, DOI: **10.1002/eom2.12353**.

58 D. Dilek, C. A. Sharpe and L. R. Sharpe, $LaFe_xCo_{(1-x)}O_3$ Thin-Film Oxygen Reduction Catalysts Prepared Using Spray Pyrolysis without Conductive Additives, *ACS Omega*, 2017, **2**(11), 7695–7701, DOI: **10.1021/acsomega.7b01428**.

59 G. Xiaoming, Y. Du, B. Li, T. S. Andy Hor, M. Sindoro, Y. Zong, H. Zhang and Z. Liu, Intrinsically conductive perovskite oxides with enhanced stability and electrocatalytic activity for oxygen reduction reactions, *ACS Catal.*, 2016, **6**(11), 7865–7871, DOI: **10.1021/acscatal.6b02493**.